AGU ADVANCING EARTH AND SPACE SCIENCES

Geophysical Research Letters

RESEARCH LETTER
10.1029/2024GL111873

Lateral Fluxes Drive Basal Melting Beneath Thwaites Eastern Ice Shelf, West Antarctica

Peter E. D. Davis[1], Keith W. Nicholls[1], David M. Holland[2,3], Britney E. Schmidt[4], Peter Washam[4], Bieito Fernández Castro[5], Kiya L. Riverman[6,7], James A. Smith[1], Paul G. D. Anker[1], Andrew D. Mullen[4], Daniel Dichek[4], Elisabeth Clyne[8], and Keith Makinson[1]

[1]British Antarctic Survey, Cambridge, UK, [2]Courant Institute of Mathematical Sciences, New York University, New York, NY, USA, [3]Center for Global Sea Level Change, New York University Abu Dhabi, Abu Dhabi, UAE, [4]Department of Astronomy, Cornell University, Ithaca, NY, USA, [5]School of Ocean and Earth Science, University of Southampton, Southampton, UK, [6]Department of Environmental Studies, University of Portland, Portland, OR, USA, [7]College of Earth, Ocean, and Atmospheric Sciences, Oregon State University, Corvallis, OR, USA, [8]Environmental Consulting Services, Tetra Tech Inc., Lakewood, CO, USA

Key Points:

- First observations of oceanic turbulence from the grounding line of Thwaites Eastern Ice Shelf
- Rather than the vertical turbulent heat flux, the lateral advective heat flux within 4 m of the ice base sustains the basal melt rate
- Lateral heat fluxes driven by the large-scale advective circulation likely dominate melting beneath many West Antarctica's ice shelves

Supporting Information:

Supporting Information may be found in the online version of this article.

Correspondence to:

P. E. D. Davis,
petvis@bas.ac.uk

Citation:

Davis, P. E. D., Nicholls, K. W., Holland, D. M., Schmidt, B. E., Washam, P., Castro, B. F., et al. (2025). Lateral fluxes drive basal melting beneath Thwaites Eastern Ice Shelf, West Antarctica. *Geophysical Research Letters*, *52*, e2024GL111873. https://doi.org/10.1029/2024GL111873

Received 14 AUG 2024
Accepted 13 DEC 2024

Abstract Thwaites Glacier is one of the fastest-changing ice-ocean systems in Antarctica. Basal melting beneath Thwaites' floating ice shelf, especially around pinning points and at the grounding line, sets the rate of ice loss and Thwaites' contribution to global sea-level rise. The rate of basal melting is controlled by the transport of heat into and through the ice–ocean boundary layer toward the ice base. Here we present the first turbulence observations from the grounding line of Thwaites Eastern Ice Shelf. We demonstrate that contrary to expectations, the turbulence-driven vertical flux of heat into the ice–ocean boundary layer is insufficient to sustain the basal melt rate. Instead, most of the heat required must be delivered by lateral fluxes driven by the large-scale advective circulation. Lateral processes likely dominate beneath the most unstable warm-cavity ice shelves, and thus must be fully incorporated into parameterizations of ice shelf basal melting.

Plain Language Summary Our knowledge of the response of Thwaites Glacier to the changing climate of the 21st century remains highly uncertain despite the significant risk it poses to global sea-level if it were to collapse entirely. The rate of ice loss from Thwaites over at least the next 100 years will be controlled by the rate at which its ice shelf—the portion of the glacier that floats on the ocean—is melted from below by 'warm' ocean water. Understanding the processes that drive this basal melting is therefore essential. Here we present the first observations of vertical mixing and small-scale ocean turbulence right at the critical point that Thwaites Glacier first begins to float (referred to as the grounding line). Unexpectedly, we find that the heat required to maintain basal melting is not brought to the ice base via vertical mixing, but rather it is delivered horizontally via the large-scale ocean circulation. The dominance of lateral processes is likely to be important for many of Antarctica's most unstable glaciers which overlie warm ocean water, and therefore must be fully incorporated into models of basal melting to reliably predict the rate of future sea-level rise.

1. Introduction

Thwaites Glacier is poised to be the single largest West Antarctic contributor to global sea-level rise over the 21st century (Bett et al., 2024). Grounded below sea-level on a retrograde bed (Fretwell et al., 2013), Thwaites is responsible for draining 10% of the West Antarctic Ice Sheet (Rignot et al., 2019; Scambos et al., 2017) and is highly susceptible to marine ice sheet instabilities (Bradley & Hewitt, 2024; Joughin et al., 2014; Yu et al., 2019). In some regions its grounding line, the point where the glacier first goes afloat, has retreated 14 km inland since the late 1990s, and is currently retreating by up to 1.2 km per year (Milillo et al., 2019). Thwaites may already have entered a period of rapid and irreversible ice loss (Bett et al., 2024; Joughin et al., 2014), and would contribute >65 cm to global sea-level if it were to collapse entirely (Morlighem et al., 2020).

Ice loss from Thwaites (and other major West Antarctic outlet glaciers) and whether it proceeds irreversibly is dynamically linked to the rate of ice shelf basal melting around pinning points (Bett et al., 2024) and at the grounding line (Arthern & Williams, 2017). Melt-induced ice shelf thinning in these regions results in a loss of ice shelf buttressing, leading to higher spreading stresses, faster flow and dynamic thinning of grounded ice upstream (Alley et al., 2021; Reese et al., 2018; Wild et al., 2022). As this thinner ice goes afloat, the ice shelf increasingly ungrounds from pinning points and the grounding line retreats inland, further accelerating the flux of grounded ice

into the ocean. Moreover, strong geometric feedbacks exist whereby basal melt-induced ice shelf thinning opens new areas of sub-ice shelf cavity, promoting further basal melting and grounding line retreat (Bett et al., 2024; Bevan et al., 2021; P. R. Holland et al., 2023). Ocean-driven basal melting is currently accelerating beneath Thwaites: between 1994 and 2012, the rate of ice shelf mass loss in West Antarctica has increased by 70% (Paolo et al., 2015), while associated grounded ice discharge has increased by 77% between 1973 and 2009, with half the increase occurring between 2003 and 2009 (Mouginot et al., 2014).

The rate of ice shelf basal melting is controlled by the divergence at the ice–ocean boundary between the conductive heat flux into the ice and the oceanic heat flux across the phase change interface (Jenkins et al., 2010; Supplementary Figure S1 in Supporting Information S1)

$$\rho_i a_b L_i = Q_i^T + Q_b^T, \tag{1}$$

where ρ is density, a_b the basal melt rate, L the latent heat of fusion, T the temperature, Q_b^T the ocean heat flux and $Q_i^T = \rho_i c_i \kappa_i \frac{\partial T_i}{\partial z}\Big|_b$ the conductive heat flux into the ice where c is the specific heat capacity, z the depth, and κ the thermal diffusivity. The subscripts i and b refer to ice and ice–ocean boundary, respectively. In turn, Q_b^T is maintained by ocean processes fluxing heat into and through the ice shelf ocean boundary layer, which beneath Thwaites Eastern Ice Shelf (TEIS) is assumed to be ∼2 m thick (Figure 1b). Beneath cold, tidally driven ice shelves, this flux is predominantly vertical and is driven by shear generated turbulence (Davis & Nicholls, 2019; Jenkins et al., 2010). In coarse ice shelf cavity-scale models that don't resolve the turbulent processes directly, it is parameterized through the canonical "three-equation model" (D. M. Holland & Jenkins, 1999) which assumes Q_b^T is a purely vertical process linearly related to the difference between the far-field and boundary temperature and the far-field flow speed (i.e., $Q_b^T \propto \overline{u}_\infty (T_\infty - T_b)$; Jenkins et al., 2010). This far-field depth can be 10s of meters from the ice base (Gwyther et al., 2020; Losch, 2008). For ice shelves floating in warm water, or water with weak currents, the standard three-equation formalism is known to perform poorly. Where stratification dominates, such as beneath TEIS, shear-driven turbulence is suppressed (Vreugdenhil & Taylor, 2019), and the three-equation model substantially overestimates the melt rate for a given far-field temperature (Davis et al., 2023). Furthermore, the dynamics of lateral versus vertical melting in these environments is entirely unaccounted for (Schmidt et al., 2023). Where double-diffusive processes are important, stratification acts to enhance rather than suppress turbulence (Middleton et al., 2021; Rosevear et al., 2021), and the assumptions in the three-equation model are no longer valid (Middleton et al., 2022). Developing improved basal melt parameterizations for stratified warm cavity ice shelves where the rate of ice mass loss is generally greatest is a central effort to reducing uncertainty in 21st century sea-level projections.

In this letter we highlight a further limitation of the standard formulation of the three-equation model: namely that parameterizing Q_b^T solely as a vertical process neglects a substantial proportion of the heat flux that drives basal melting. Using turbulence data collected by a Rockland Scientific International (RSI) Velocity Microstructure Profiler (VMP) at the grounding line beneath TEIS (Section 2), we demonstrate that ∼80% of the heat flux required to maintain basal melting is sourced from horizontal advection within 4 m of the ice base (Section 3). The predominance of lateral advection is likely to be a consistent feature of warm-cavity ice shelves where the ocean temperature is substantially above the in-situ freezing point (Section 4), and thus it is essential to fully quantify its impact in parameterizations of ice shelf basal melting.

2. Turbulence Observations: χ and ε

An access hole was drilled using hot water through 587 m of ice ∼1.5–2.0 km downstream of the grounding line in the "butterfly" region of TEIS (Figure 1a). Despite the quiescent ocean environment (Figures 1b and 1c, Supplementary Figure S2 in Supporting Information S1; Davis et al., 2023; Schmidt et al., 2023), there is clear evidence of vertical mixing. Persistent, high-frequency variability in the vertical temperature gradient is observed between 518 and 540 m depth (Figure 1d), and the average extent of density overturns characterized by the Thorpe Scale (A. A. Gargett & Garner, 2008) reaches 0.3 ± 0.2 m, with a maximum >1.5 m (Figure 1e). The rate of turbulent mixing was observed using an RSI VMP-250. Five full water column freefall profiles at ∼0.60–0.65 m/s were taken over a period of 20 hr between 10th–11th January 2020 (Figure 1d). The VMP was equipped with two shear probes and one fast-response thermistor sampling at 512 Hz. Both shear probes were dominated by noise

10.1029/2024GL111873

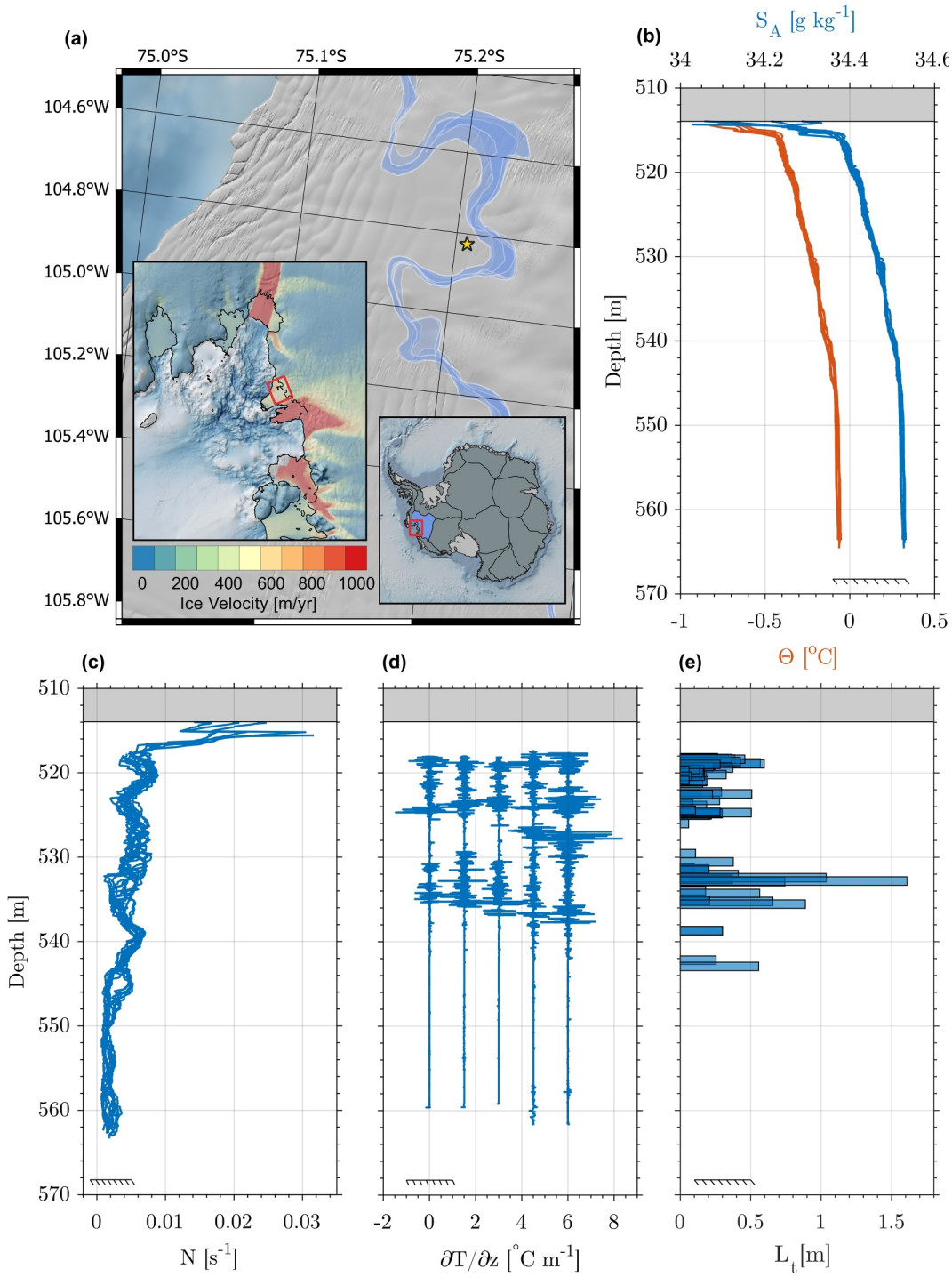

Figure 1. (a) Map of study area showing the location of the hot water drilled access hole (yellow star) in the "butterfly" region of TEIS. The blue shaded polygons show the location of the grounding line between 2016 and 2017 from Milillo et al. (2019) (b), (c), (d), (e) Vertical profiles of (b) temperature (red) and salinity (blue); (c) buoyancy frequency; (d) vertical temperature gradient; and (e) Thorpe scale density overturns at the location of the access hole. The gray box in (b, c, d, e) marks the location of the ice base, while the slash-backed black line shows the location of the seabed. The vertical temperature gradient profiles in (d) have been successively offset by +1.5°C m^{-1}.

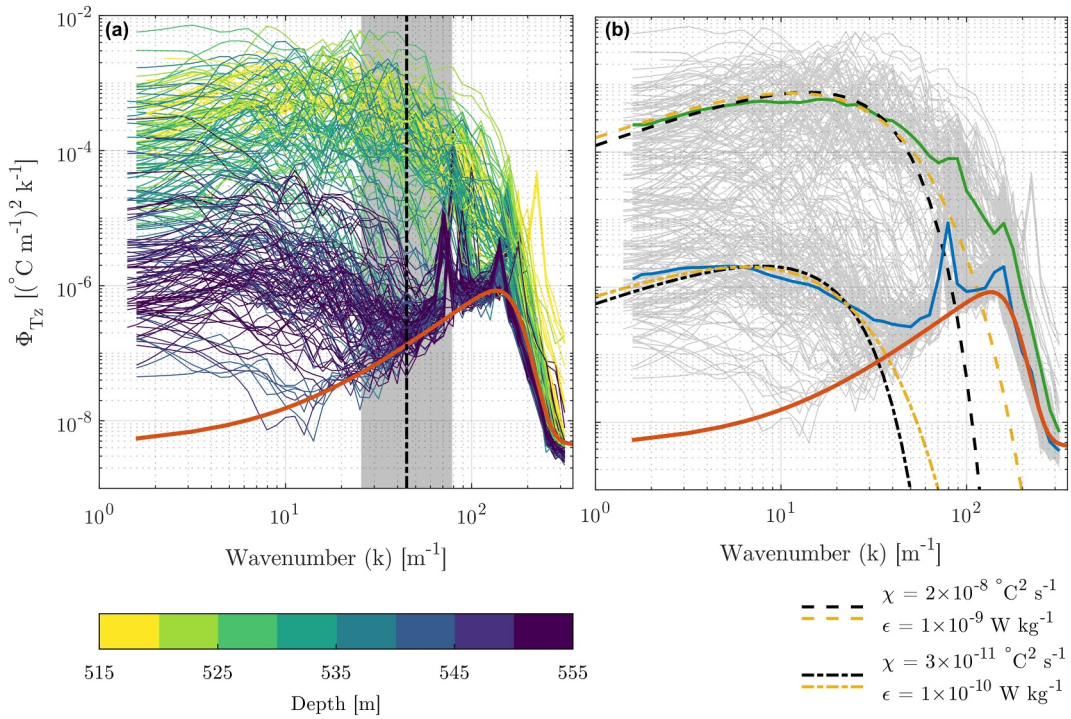

Figure 2. (a) Vertical temperature gradient wavenumber spectra beneath TEIS colored by depth. The black dot-dashed line shows the mean upper integration wavenumber while the gray envelope shows the spread given by the geometric standard deviation factor. (b) Mean low (blue; depth >545 m) and high (green; depth <525 m) energy vertical temperature gradient wavenumber spectra. Both the high and low energy spectra are well represented by the Batchelor (black dashed and dot-dashed) and Kraichnan (yellow dashed and dot-dashed) spectra. The thick red lines in (a), (b) show the mean noise spectrum.

(possibly sourced from interference with the hot water drill), leaving only high-quality thermistor data. Nevertheless, in low-energy environments, such as that beneath TEIS, thermistor-derived temperature gradient spectra (Figure 2a) alone can be used to estimate the rate of thermal variance dissipation (χ) and the rate of turbulent kinetic energy dissipation (ϵ) by utilizing the theoretical Batchelor and Kraichnan temperature gradient spectra (Figure 2b; Bluteau et al., 2017; Peterson & Fer, 2014; Piccolroaz et al., 2021; Supplementary Text S1 in Supporting Information S1). In total, 221 half-overlapped estimates of χ and ϵ were derived. Unless otherwise noted, throughout this letter we average quantities that span many orders of magnitude using a trimmed (central 90% of the data) geometric mean (Scheifele et al., 2018).

Observed temperature gradient spectra span a wide range of turbulence levels, from the quiescent lower half of the water column to the more energetic region near the ice base (Figure 2a), and are well characterized by the Batchelor or Kraichnan theoretical temperature gradient spectra (Figure 2b). Below 540 m depth, χ and ϵ are largely less than 10^{-10}°C^2 s^{-1} and 10^{-9} W kg^{-1}, respectively (Figures 3a and 3b), equivalent to open-ocean background values or the values seen in other quiescent ice shelf cavities where turbulent mixing is suppressed (Davis et al., 2022; Kimura et al., 2016). Above 540 m, ϵ and χ rapidly increase by several orders of magnitude (Figures 3a and 3b), indicating the presence of stronger turbulence despite the stronger stratification (Figure 1c; Supplementary Text S2 in Supporting Information S1). ϵ reaches 10^{-7} W kg^{-1}, and at two depths, values of ϵ derived using the Kraichnan theoretical spectra slightly exceed the maximum value of ϵ that can be reliably resolved (2×10^{-7} W kg^{-1}). χ reaches 10^{-7}°C^2 s^{-1}, and there is close agreement between the values of χ estimated using either theoretical spectrum over the full range of observed values (Figure 3c). In contrast, the Batchelor spectrum tends to underestimate the value of ϵ compared to the Kraichnan spectrum when $\epsilon > 10^{-8}$ W kg^{-1}. The difference never exceeds a factor of 2.8 (consistent with a typical factor of two uncertainty in the data $\sqrt{2^2+2^2} = 2.8$; Peterson & Fer, 2014), and therefore we do not consider it to be significant. Throughout the remainder of this letter, we use a single vertical profile of ϵ and χ derived from the average of the Batchelor and Kraichnan profiles.

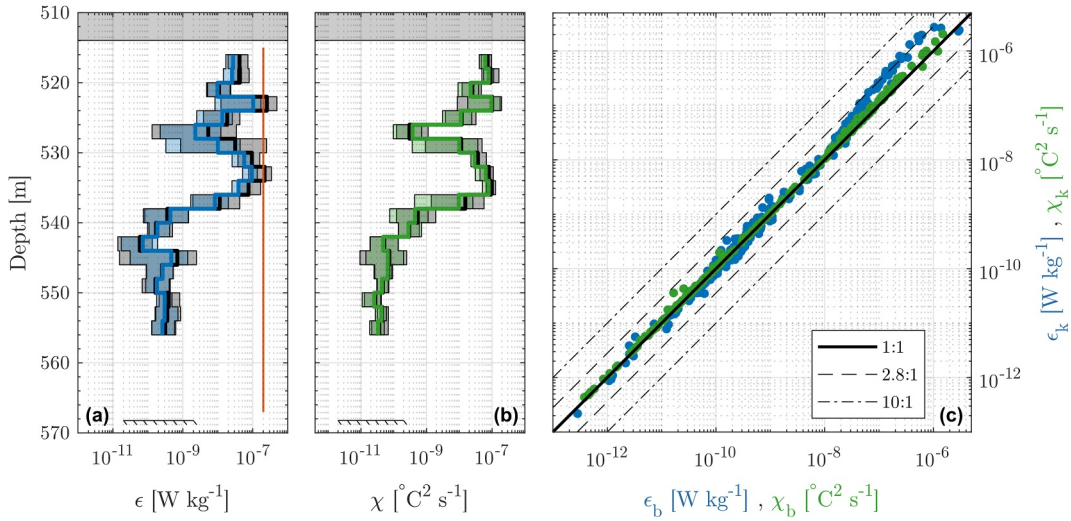

Figure 3. Mean vertical profiles of (a) ε and (b) χ averaged in 2-m vertical bins with 95% error bars derived according to Rippeth and Inall (2002). The blue and green profiles and error bars are derived using the Batchelor spectrum, while the black profiles and gray error bars are derived using the Kraichnan spectrum. The gray box in (a), (b) marks the location of the ice base, while the slash-backed black line shows the location of the seabed. The red line in (a) shows the maximum value of ε that can be resolved with $H_f = 10$. (c) Comparison between ε (blue) and χ (green) values estimated using the Batchelor (x axis) and Kraichnan (y axis) theoretical spectra.

3. Vertical Scalar Diffusivity and Vertical Heat Flux

The vertical ocean heat flux Q_w^T is calculated from the vertical scalar diffusivity K_ρ and the large-scale vertical temperature gradient $\partial\overline{T}/\partial z$

$$Q_w^T = \rho_w c_w K_\rho \frac{\partial \overline{T}}{\partial z}, \tag{2}$$

where the subscript w refers to the ocean. K_ρ is sensitive to the balance between the strength of oceanic turbulence (Figures 3a and 3b) and the vertical density stratification (Figure 1c). This balance can be represented through the buoyancy Reynolds number

$$Re_b = \varepsilon/\nu N^2, \tag{3}$$

which quantifies the ratio between the destabilizing effect of turbulence to the stabilizing effect of viscosity and stratification (given by the buoyancy frequency N; Bouffard & Boegman, 2013). The value of Re_b beneath TEIS varies by orders of magnitude, indicating the presence of multiple mixing regimes (Figure 4a; Barry et al., 2001). Above 536 m depth, Re_b is close to or above 400, indicative of the presence of fully developed, isotropic, high Reynolds number turbulence that is unaffected by stratification (A. E. Gargett et al., 1984). Below 536 m depth, Re_b decreases, consistent with the rapid reduction in turbulence strength (Figures 3a and 3b), and between 540 and 546 m depth, $Re_b < \sim 15$ which marks the boundary below which turbulent mixing is largely weak, anisotropic and limited by vertical stratification.

Many parameterizations exist for estimating K_ρ. Here we use three separate methods: Osborn (1980; OSB), Osborn and Cox (1972; OC) and Bouffard and Boegman (2013; BB). The OSB and OC methods are widely used and relate the vertical diffusivity to ε

$$K_\rho = 0.2\frac{\varepsilon}{N^2}, \tag{4}$$

where 0.2 is a constant mixing efficiency, or to the rate of suppression of scalar variance χ, respectively

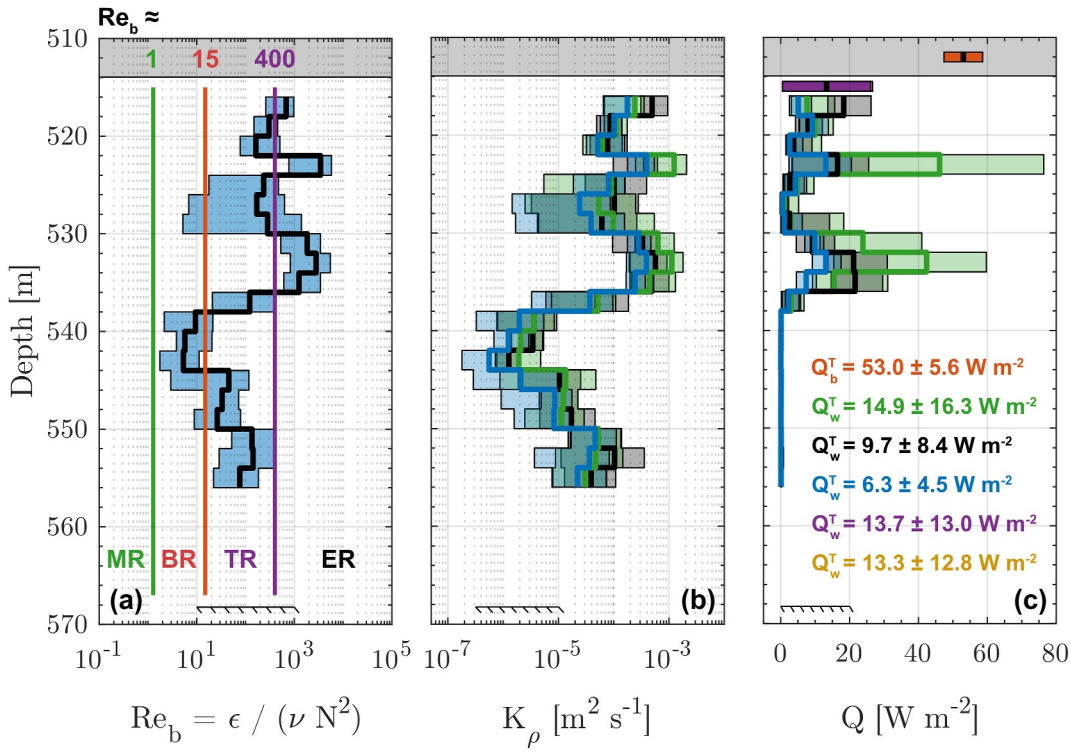

Figure 4. Mean vertical profiles of (a) buoyancy Reynolds number; (b) vertical diffusivity; and (c) vertical heat flux (b), (c) The green, black, and blue profiles are derived using the Osborn, Osborn-Cox and Bouffard and Boegman models, respectively. The gray box in each panel marks the location of the ice base, while the slash-backed black line shows the location of the seabed. The green, red, and purple lines in (a) mark the upper boundaries of the molecular (MR), buoyancy controlled (BR) and transitional (TR) regimes. ER indicates the energetic regime. The purple and yellow boxes (indistinguishable) in (c) show the vertical heat flux calculated from the turbulence instrument cluster using the Osborn and Bouffard and Boegman models, respectively. The red box shows the magnitude of the vertical heat flux required to sustain the observed rate of ice shelf basal melting. The vertical heat flux required to sustain the basal melt rate, as well as the arithmetic mean vertical heat flux derived from each individual method used to calculate K_ρ (color-coded) is shown in panel (c).

$$K_\rho = \frac{\chi}{2\left(\partial \overline{T}/\partial z\right)^2}. \tag{5}$$

The BB method utilizes the buoyancy Reynolds number and the turbulent Prandtl number to quantify K_ρ across all mixing regimes (see Table 2 in Bouffard & Boegman, 2013). None of these methods are valid in the presence of a solid boundary. However, as the length-scale of the turbulence (L_T = 0.5 m; Figure 1d) at our shallowest observation depth (~518 m) is less than the distance to the boundary (4 m), the use of these methods remains valid. The minimum value of K_ρ is the molecular diffusivity of heat ($\kappa_T = 1.4 \times 10^{-7}$ m^2 s^{-1}). The diffusivity calculated using all methods is broadly similar (Figure 4b), ranging from 10^{-7} m^2 s^{-1} in the buoyancy-controlled regime to 10^{-4} m^2 s^{-1} in the energetic regime. Where the turbulent intensity is greatest (e.g. z = 522 m or z = 532–534 m), the diffusivity calculated via OSB and OC exceeds that calculated via BB. Bouffard and Boegman (2013) argue that both the OSB and OC methods can become unreliable in the energetic regime, as the mixing efficiency decreases compared to the constant 0.2 value in the OSB model, and $\partial \overline{T}/\partial z$ tends to zero in the OC model.

Below 538 m depth, the large-scale vertical temperature gradient is zero (Figure 1b), and therefore Q_w^T is zero (Figure 4c). Above 538 m, however, Q_w^T becomes non-zero with an arithmetic mean value across all diffusivity methods of 10.4 ± 11.3 W m^{-2}. Our results show that irrespective of the method used to calculate K_ρ, Q_w^T is insufficient to sustain the ice-ocean boundary heat flux (Q_b^T = 53.0 ± 5.6 W m^{-2}; Supplementary Figure S1 in Supporting Information S1) that is required to maintain the average rate of basal melting beneath TEIS (a_b = 5.4 ± 0.6 m yr^{-1}; Davis et al., 2023) when $Q_i^T = -0.95$ W m^{-2} (Equation 1). Where K_ρ is largest in the

energetic regime, Q_w^T can exceed 40 W m^{-2} for the OSB and OC models (Figure 4c), but these depth-limited spikes cannot sustain a constant vertical supply of heat. Instead, additional processes must be responsible for delivering the sustained supply of heat to the ice base required to drive basal melting.

4. Conclusions and Implications: Heat Balance at the Ice–Ocean Interface

In this letter we have presented the first observations of oceanic turbulence near the grounding line beneath TEIS (Figure 1). Using the vertical temperature gradient wavenumber spectra (Figure 2) we observe that turbulence intensity shows considerable variability, with the rate of turbulent kinetic energy dissipation (ϵ) and the rate of thermal variance dissipation (χ) varying by orders of magnitude (Figure 3). The interplay between the strength of the turbulence and the vertical density stratification as quantified by the buoyancy Reynolds number (Figure 4a) spans the full range of mixing environments. Three independent models of the vertical diffusivity (Figure 4b) are used along with the large-scale vertical temperature gradient to derive the vertical heat flux (Q_w^T; Figure 4c), which reaches an arithmetic mean value of 10.4 ± 11.3 W m^{-2} between 4 and 24 m from the ice.

The average rate of basal melting at the grounding line of TEIS (5.4 ± 0.6 m yr^{-1}) requires a sustained vertical heat flux Q_b^T across the molecular sublayer at the ice–ocean interface of 53.0 ± 5.6 W m^{-2}. As the vertical diffusivity of heat in the sublayer is fixed at molecular values, the magnitude of the heat flux is controlled entirely by the sublayer vertical temperature gradient. The flux of heat into and through the turbulent ice–ocean boundary layer must therefore match the melting flux at the ice-ocean interface, such that a sufficiently sharp temperature gradient is sustained across the molecular sublayer. Any surplus or deficit in the flux of heat to the base of the molecular sublayer will lead to a strengthening or weakening of the sublayer temperature gradient and a concomitant increase or decrease in the basal melt rate.

The rate of change of temperature ($\partial T/\partial t$) for any water column layer in an ice shelf cavity (excluding entrainment) is given by

$$h\frac{\partial T}{\partial t} = -\mathrm{h}(\mathrm{u}.\nabla T) + \left(K_\rho \frac{\partial T}{\partial z}\right)_{z=-h}, \tag{6}$$

where h is the thickness of the layer beneath the ice and the first term on the right-hand side is the horizontal advection of heat into the layer by eddies and the mean flow, and the second term on the right-hand side is the vertical heat flux across the base of the layer (Q_w^T). Considering the full water column at the borehole ($h = 54$ m), the vertical flux of heat through the seabed is zero, and thus all heat required to drive basal melting must be delivered via the large-scale circulation that advects heat toward the grounding line. As the ice base is approached, however, and layer thickness h decreases, it is typically assumed that the magnitude of the advective term becomes smaller, and Q_w^T across the base of the layer becomes increasingly dominant. Our results demonstrate that this is not the case beneath TEIS. At the borehole location, the arithmetic mean VMP-derived vertical heat flux (10.4 W m^{-2}) within 4 m of the ice base can only provide ∼20% of the heat to the base of the molecular sublayer that is required to maintain the rate of basal melting (53.0 W m^{-2}; Supplementary Figure S1 in Supporting Information S1). The remainder must be provided by lateral advection above this depth, which is driven by regional atmosphere-ice-ocean processes occurring outside of the ice shelf cavity (e.g., Dotto et al., 2022; Zheng et al., 2022), as double diffusive processes are weak (Davis et al., 2023). As our results only provide a snapshot over 20 hr, it is possible that Q_w^T is larger at other times. To verify if this is the case, ∼10 days of turbulence-resolving velocity data from a turbulence instrument cluster deployed 1.5 m beneath the ice base within the ice-ocean boundary layer was processed following the approach of Davis and Nicholls (2019). Q_w^T was calculated using the OSB and BB methods (purple bar in Figure 4c; Supplementary Figure S3 in Supporting Information S1), and the 10-day arithmetic mean was 13.7 ± 13.0 and 13.3 ± 12.8 W m^{-2}, respectively, with only 1% of the individual the heat flux measurements exceeding 53 W m^{-2}. This analysis confirms that Q_w^T is not substantially larger at other times, corroborating our assessment that Q_w^T alone cannot sustain the supply of heat required to maintain the rate of basal melting. Although outside the depth range of our observations, our results suggest that Q_w^T must increase rapidly in the last meter of the ice-ocean boundary layer, such that $Q_w^T = Q_b^T$ at the base of the molecular sublayer (Supplementary Figure S1 in Supporting Information S1). This rapid increase can only be maintained by the lateral heat convergence occurring within 4 m of the ice base, as the magnitude of Q_w^T deeper in

the water column is insufficient to maintain this balance on its own. Thus, the lateral advective heat flux and the variability therein is responsible for driving basal melting beneath TEIS.

The formulation of the turbulence closure scheme used in the canonical three-equation model assumes that there is no horizontal flux of heat above the far-field depth, and the heat required to maintain the rate of basal melting above this depth is solely delivered through the vertical heat flux (Jenkins et al., 2010). In coarse resolution, cavity-scale resolving models, this far-field depth can be 10s of meters from the ice base (Gwyther et al., 2020; Losch, 2008), and thus the three-equation model as generally applied cannot resolve the key lateral processes we have identified that are responsible for maintaining the heat balance at the ice-ocean interface. Our results imply that in regions such as beneath TEIS where horizontal processes play a critical role, the far-field depth in the three-equation model must be $\ll$ O(10) m in order to capture the necessary advective dynamics, although the exact resolution required will depend on the properties of the boundary layer, turbulence levels, and the large-scale ocean circulation. This vertical resolution is hard to achieve in large-scale models, so parameterizations of these advective dynamics is critical.

Conceptually the predominance of lateral heat fluxes makes sense when considering the magnitude of thermal driving (difference between the in-situ ocean temperature and freezing point) beneath TEIS. At a depth less than 0.1 m from the ice the thermal driving exceeds 1.5°C, indicating that horizontal delivery of heat by the large-scale advective circulation far exceeds that required to maintain basal melting along the inflow pathway. Indeed, Davis et al. (2023) demonstrated that the melt rate beneath TEIS is highly suppressed by the strong stratification and quiescent ocean conditions, and therefore we can conclude that much of the heat delivered through horizontal advection remains unable to access the ice base. That is, at and above the depth in the ice-ocean boundary layer where Q_w^T must equal Q_b^T, the stratification associated with the freshwater layer that pools along the relatively flat ice base strongly limits the turbulence intensity and vertical mixing, and ultimately caps the amount of energy for basal melting that can be extracted from the large reservoir of heat provided by lateral advection. While the importance of lateral fluxes is likely to diminish in cold-cavity ice shelves where the temperature of the shear-driven, well-mixed ice–ocean boundary layer is close to freezing and the heat required to drive melting can only be sourced vertically from warmer layers below, it is likely to dominate in warm cavity ice shelves with elevated thermal driving and a surplus of heat provided by the large-scale circulation. Thus, our results from beneath TEIS can be more broadly generalized to Antarctica's full range of warm-cavity ice shelves. The future behavior of ocean-driven basal melting beneath these ice shelves is intricately linked to the rate and extent of ice loss from Antarctica and thus global sea-level rise. Global sea-level rise is one of the most urgent socioeconomic issues facing humanity, and thus it is imperative that lateral heat fluxes are fully quantified in parameterizations of ice shelf basal melting and ultimately our projections of future ice loss.

Data Availability Statement

The CTD data used in Figure 1b,1c,1e are available from the UK Polar Data Centre via Davis et al. (2021a). The ApRES data from which the mean melt rate is derived are available from the UK Polar Data Centre via Davis et al. (2021b). The VMP data are available from the UK Polar Data Centre via Davis et al. (2024).

Acknowledgments
This work is from the MELT project, a component of the International Thwaites Glacier Collaboration. Support from National Science Foundation (NSF: Grant 1739003) and Natural Environment Research Council (NERC: Grant NE/S006656/1). Logistics provided by NSF-U. S. Antarctic Program and NERC-British Antarctic Survey. International Thwaites Glacier Collaboration Contribution No. ITGC-133.

References

Alley, K. E., Wild, C. T., Luckman, A., Scambos, T. A., Truffer, M., Pettit, E. C., et al. (2021). Two decades of dynamic change and progressive destabilization on the Thwaites Eastern Ice Shelf. *The Cryosphere*. https://doi.org/10.5194/tc-2021-76

Arthern, R. J., & Williams, C. R. (2017). The sensitivity of West Antarctica to the submarine melting feedback. *Geophysical Research Letters*, *44*(5), 2352–2359. https://doi.org/10.1002/2017GL072514

Barry, M. E., Ivey, G. N., Winters, K. B., & Imberger, J. (2001). Measurements of diapycnal diffusivities in stratified fluids. *Journal of Fluid Mechanics*, *442*, 267–291. https://doi.org/10.1017/S0022112001005080

Bett, D. T., Bradley, A. T., Williams, C. R., Holland, P. R., Arthern, R. J., & Goldberg, D. N. (2024). Coupled ice/ocean interactions during the future retreat of West Antarctic ice streams. https://doi.org/10.5194/tc-2023-77

Bevan, S. L., Luckman, A. J., Benn, D. I., Adusumilli, S., & Crawford, A. (2021). Brief communication: Thwaites Glacier cavity evolution. *The Cryosphere*, *15*(7), 3317–3328. https://doi.org/10.5194/tc-15-3317-2021

Bluteau, C. E., Lueck, R. G., Ivey, G. N., Jones, N. L., Book, J. W., & Rice, A. E. (2017). Determining mixing rates from concurrent temperature and velocity measurements. *Journal of Atmospheric and Oceanic Technology*, *34*(10), 2283–2293. https://doi.org/10.1175/JTECH-D-16-0250.1

Bouffard, D., & Boegman, L. (2013). A diapycnal diffusivity model for stratified environmental flows. *Dynamics of Atmospheres and Oceans*, *61–62*, 14–34. https://doi.org/10.1016/j.dynatmoce.2013.02.002

Bradley, A. T., & Hewitt, I. J. (2024). Tipping point in ice-sheet grounding-zone melting due to ocean water intrusion. *Nature Geoscience*, *17*(7), 631–637. https://doi.org/10.1038/s41561-024-01465-7

Davis, P. E. D., Jenkins, A., Nicholls, K. W., Dutrieux, P., Schröder, M., Janout, M. A., et al. (2022). Observations of modified warm deep water beneath ronne ice shelf, Antarctica, from an autonomous underwater vehicle. *Journal of Geophysical Research: Oceans*, *127*(11). https://doi.org/10.1029/2022JC019103

Davis, P. E. D., & Nicholls, K. W. (2019). Turbulence observations beneath larsen C ice shelf, Antarctica. *Journal of Geophysical Research*, *124*(8), 5529–5550. https://doi.org/10.1029/2019JC015164

Davis, P. E. D., Nicholls, K. W., & Holland, D. M. (2021a). Thwaites MELT: Conductivity, temperature and depth (CTD) profiles from the grounding zone region of Thwaites Glacier eastern ice shelf (2020) (version 1.0). *UK Polar Data Centre, Natural Environment Research Council, UK Research & Innovation*. [Dataset]. https://doi.org/10.5285/97204415-683F-4D55-8B38-A2700FA94EFE

Davis, P. E. D., Nicholls, K. W., & Holland, D. M. (2021b). Thwaites MELT: Temperature, salinity and velocity time series from the grounding zone region of Thwaites Glacier Eastern ice shelf (2020) (Version 1.0). *UK Polar Data Centre, Natural Environment Research Council, UK Research & Innovation*. [Dataset]. https://doi.org/10.5285/4FFAD557-1C3C-4EA7-A73D-6D782331B08A

Davis, P. E. D., Nicholls, K. W., & Holland, D. M. (2024). Thwaites MELT: Velocity microstructure profiles from the grounding zone region of Thwaites Glacier eastern ice shelf (2020) (version 1.0). *UK Polar Data Centre, Natural Environment Research Council, UK Research & Innovation*. [Dataset]. https://doi.org/10.5285/2B33895B-5069-4C49-95BD-2624C980498B

Davis, P. E. D., Nicholls, K. W., Holland, D. M., Schmidt, B. E., Washam, P., Riverman, K. L., et al. (2023). Suppressed basal melting in the eastern Thwaites Glacier grounding zone. *Nature*, *614*(7948), 479–485. https://doi.org/10.1038/s41586-022-05586-0

Dotto, T. S., Heywood, K. J., Hall, R. A., Scambos, T. A., Zheng, Y., Nakayama, Y., et al. (2022). Ocean variability beneath Thwaites eastern ice shelf driven by the pine island bay gyre strength. *Nature Communications*, *13*(1), 7840. https://doi.org/10.1038/s41467-022-35499-5

Fretwell, P., Pritchard, H. D., Vaughan, D. G., Bamber, J. L., Barrand, N. E., Bell, R., et al. (2013). Bedmap2: Improved ice bed, surface and thickness datasets for Antarctica. *The Cryosphere*, *7*(1), 375–393. https://doi.org/10.5194/tc-7-375-2013

Gargett, A., & Garner, T. (2008). Determining Thorpe scales from ship-lowered CTD density profiles. *Journal of Atmospheric and Oceanic Technology*, *25*(9), 1657–1670. https://doi.org/10.1175/2008JTECHO541.1

Gargett, A. E., Osborn, T. R., & Nasmyth, P. W. (1984). Local isotropy and the decay of turbulence in a stratified fluid. *Journal of Fluid Mechanics*, *144*, 231–280. https://doi.org/10.1017/S0022112084001592

Gwyther, D. E., Kusahara, K., Asay-Davis, X. S., Dinniman, M. S., & Galton-Fenzi, B. K. (2020). Vertical processes and resolution impact ice shelf basal melting: A multi-model study. *Ocean Modelling*, *147*, 101569. https://doi.org/10.1016/j.ocemod.2020.101569

Holland, D. M., & Jenkins, A. (1999). Modeling thermodynamic ice–ocean interactions at the base of an ice shelf. *Journal of Physical Oceanography*, *29*(8), 1787–1800. https://doi.org/10.1175/1520-0485(1999)029<1787:MTIOIA>2.0.CO;2

Holland, P. R., Bevan, S. L., & Luckman, A. J. (2023). Strong Ocean melting feedback during the recent retreat of Thwaites Glacier. *Geophysical Research Letters*, *50*(8), e2023GL103088. https://doi.org/10.1029/2023GL103088

Jenkins, A., Nicholls, K. W., & Corr, H. F. J. (2010). Observation and parameterization of ablation at the base of ronne ice shelf, Antarctica. *Journal of Physical Oceanography*, *40*(10), 2298–2312. https://doi.org/10.1175/2010JPO4317.1

Joughin, I., Smith, B. E., & Medley, B. (2014). Marine ice sheet collapse potentially under way for the Thwaites Glacier basin, west Antarctica. *Science*, *344*(6185), 735–738. https://doi.org/10.1126/science.1249055

Kimura, S., Jenkins, A., Dutrieux, P., Forryan, A., Naveira Garabato, A. C., & Firing, Y. (2016). Ocean mixing beneath pine Island glacier ice shelf, west Antarctica. *Journal of Geophysical Research*, *121*(12), 8496–8510. https://doi.org/10.1002/2016JC012149

Losch, M. (2008). Modeling ice shelf cavities in a z coordinate ocean general circulation model. *Journal of Geophysical Research*, *113*(C8), C08043. https://doi.org/10.1029/2007JC004368

Middleton, L., Davis, P. E. D., Taylor, J. R., & Nicholls, K. W. (2022). Double diffusion as a driver of turbulence in the stratified boundary layer beneath george VI ice shelf. *Geophysical Research Letters*, *49*(5). https://doi.org/10.1029/2021GL096119

Middleton, L., Vreugdenhil, C. A., Holland, P. R., & Taylor, J. R. (2021). Numerical simulations of melt-driven double-diffusive fluxes in a turbulent boundary layer beneath an ice shelf. *Journal of Physical Oceanography*, *51*(2), 403–418. https://doi.org/10.1175/JPO-D-20-0114.1

Milillo, P., Rignot, E., Rizzoli, P., Scheuchl, B., Mouginot, J., Bueso-Bello, J., & Prats-Iraola, P. (2019). Heterogeneous retreat and ice melt of Thwaites Glacier, west Antarctica. *Science Advances*, *5*(1), eaau3433. https://doi.org/10.1126/sciadv.aau3433

Morlighem, M., Rignot, E., Binder, T., Blankenship, D., Drews, R., Eagles, G., et al. (2020). Deep glacial troughs and stabilizing ridges unveiled beneath the margins of the Antarctic ice sheet. *Nature Geoscience*, *13*(2), 132–137. https://doi.org/10.1038/s41561-019-0510-8

Mouginot, J., Rignot, E., & Scheuchl, B. (2014). Sustained increase in ice discharge from the Amundsen sea embayment, west Antarctica, from 1973 to 2013. *Geophysical Research Letters*, *41*(5), 1576–1584. https://doi.org/10.1002/2013GL059069

Osborn, T. R. (1980). Estimates of the local rate of vertical diffusion from dissipation measurements. *Journal of Physical Oceanography*, *10*(1), 83–89. https://doi.org/10.1175/1520-0485(1980)010<0083:EOTLRO>2.0.CO;2

Osborn, T. R., & Cox, C. S. (1972). Oceanic fine structure. *Geophysical Fluid Dynamics*, *3*(4), 321–345. https://doi.org/10.1080/03091927208236085

Paolo, F. S., Fricker, H. A., & Padman, L. (2015). Volume loss from Antarctic ice shelves is accelerating. *Science*, *348*(6232), 327–331. https://doi.org/10.1126/science.aaa0940

Peterson, A. K., & Fer, I. (2014). Dissipation measurements using temperature microstructure from an underwater glider. *Methods in Oceanography*, *10*, 44–69. https://doi.org/10.1016/j.mio.2014.05.002

Piccolroaz, S., Fernández-Castro, B., Toffolon, M., & Dijkstra, H. A. (2021). A multi-site, year-round turbulence microstructure atlas for the deep perialpine Lake Garda. *Scientific Data*, *8*(1), 188. https://doi.org/10.1038/s41597-021-00965-0

Reese, R., Gudmundsson, G. H., Levermann, A., & Winkelmann, R. (2018). The far reach of ice-shelf thinning in Antarctica. *Nature Climate Change*, *8*(1), 53–57. https://doi.org/10.1038/s41558-017-0020-x

Rignot, E., Mouginot, J., Scheuchl, B., van den Broeke, M., van Wessem, M. J., & Morlighem, M. (2019). Four decades of Antarctic ice sheet mass balance from 1979–2017. *Proceedings of the National Academy of Sciences*, *116*(4), 1095–1103. https://doi.org/10.1073/pnas.1812883116

Rippeth, T. P., & Inall, M. E. (2002). Observations of the internal tide and associated mixing across the Malin Shelf. *Journal of Geophysical Research*, *107*(C4), 3028. https://doi.org/10.1029/2000JC000761

Rosevear, M. G., Gayen, B., & Galton-Fenzi, B. K. (2021). The role of double-diffusive convection in basal melting of Antarctic ice shelves. *Proceedings of the National Academy of Sciences*, *118*(6), e2007541118. https://doi.org/10.1073/pnas.2007541118

Scambos, T. A., Bell, R. E., Alley, R. B., Anandakrishnan, S., Bromwich, D. H., Brunt, K., et al. (2017). How much, how fast? A science review and outlook for research on the instability of Antarctica's Thwaites Glacier in the 21st century. *Global and Planetary Change*, *153*, 16–34. https://doi.org/10.1016/j.gloplacha.2017.04.008

Scheifele, B., Waterman, S., Merckelbach, L., & Carpenter, J. R. (2018). Measuring the dissipation rate of turbulent kinetic energy in strongly stratified, low-energy environments: A case study from the Arctic ocean. *Journal of Geophysical Research: Oceans*, *123*(8), 5459–5480. https://doi.org/10.1029/2017JC013731

Schmidt, B. E., Washam, P., Davis, P. E. D., Nicholls, K. W., Holland, D. M., Lawrence, J. D., et al. (2023). Heterogeneous melting near the Thwaites Glacier grounding line. *Nature*, *614*(7948), 471–478. https://doi.org/10.1038/s41586-022-05691-0

Vreugdenhil, C. A., & Taylor, J. R. (2019). Stratification effects in the turbulent boundary layer beneath a melting ice shelf: Insights from resolved large-eddy simulations. *Journal of Physical Oceanography*, *49*(7), 1905–1925. https://doi.org/10.1175/JPO-D-18-0252.1

Wild, C. T., Alley, K. E., Muto, A., Truffer, M., Scambos, T. A., & Pettit, E. C. (2022). Weakening of the pinning point buttressing Thwaites Glacier, west Antarctica. *The Cryosphere*, *16*(2), 397–417. https://doi.org/10.5194/tc-16-397-2022

Yu, H., Rignot, E., Seroussi, H., Morlighem, M., & Choi, Y. (2019). Impact of iceberg calving on the retreat of Thwaites Glacier, west Antarctica over the next century with different calving laws and ocean thermal forcing. *Geophysical Research Letters*, *46*(24), 14539–14547. https://doi.org/10.1029/2019GL084066

Zheng, Y., Stevens, D. P., Heywood, K. J., Webber, B. G. M., & Queste, B. Y. (2022). Reversal of ocean gyres near ice shelves in the Amundsen Sea caused by the interaction of sea ice and wind. *The Cryosphere Discussions*. https://doi.org/10.5194/tc-2021-390